Imaging light fluence in blood vessels by combining photoacoustic fluctuation imaging and ultrasound power doppler

Ivana Falco, Emmanuel Bossy, Bastien Arnal

Imaging light fluence in blood vessels by combining photoacoustic fluctuation imaging and ultrasound power Doppler

Ivana Falco, Emmanuel Bossy, Bastien Arnal*

Univ. Grenoble Alpes, CNRS, LIPhy, 140 rue de la Physique, CS 40700, 38058 Grenoble CEDEX 9, FRANCE

*: Author to whom any correspondence should be addressed.

E-mail: bastien.arnal@univ-grenoble-alpes.fr

April 2024

Abstract. *Objectives.* Numerous optical biomedical imaging or therapeutic modalities suffer from unknown light fluence distribution at depths. Photoacoustic (PA) imaging, which enables imaging blood vessels at the acoustic resolution, probes the product between the fluence and effective optical absorption that depends on the size or density of blood vessels. In the case of unresolved vessels, fluence and absorption can not be decoupled using PA imaging alone without the use of inverse problems. Thus, we propose combining two modalities that are sensitive to blood vessels to directly image fluence maps within vascularized areas, including in unresolved vessels. *Approach.* To achieve fluence imaging, the combination of photoacoustic fluctuation (PAFI) and Ultrasound Power Doppler (UPD) images is considered. After exposing a new theoretical expression of the UPD image, we establish a fluence imaging method giving quantitative fluence in blood vessels. Fluence imaging involves resolution compensation with a PSF filter that is compared to alternative simpler corrections. *Main results.* This method universally applies to arbitrary hematocrit and multi-scale vessel imaging. Using a spherical sparse array, we demonstrate 3D fluence imaging within blood vessels in simulation and experiments which is not possible with PAFI alone. *Significance.* Overall, we show that combining PAFI and UPD has the potential for real-time light dosimetry or could enhance quantitative inverse problems in photoacoustic imaging.

Keywords : Fluence imaging; Quantitative Photoacoustic imaging; ultrasound Power Doppler; Photoacoustic fluctuation imaging; blood vessels

1. Introduction

Biological tissues strongly scatter light that reaches a diffusive regime already at shallow depths $\approx 1mm$. Numerous imaging or therapeutic approaches use diffuse light to interact with tissues such as photodynamic therapy (Kim & Darafsheh 2020), laser thermotherapy (Holmer et al. 2006), diffuse optical tomography (Hoshi & Yamada 2016) or photoacoustic imaging (Beard 2011). Predicting how much light intensity reaches a target lies within the challenges of multiple fields for dosimetry (Kim & Darafsheh 2020, Holmer et al. 2006), or for quantitative imaging aspects (Arridge 1999, Cox et al. 2009).

Photoacoustic imaging enables probing the absorbed energy (product of light fluence and optical absorption coefficient). Particularly, spectroscopic applications suffer from the spectral coloring effect resulting in inaccurate chromophore concentration determination, if not corrected (Cox et al. 2009). When assumptions on the medium can be made (homogeneous, layered...), light transport can be modeled which can result in fluence-corrected photoacoustic images (Park et al. 2019, Bu et al. 2012, Jeng et al. 2021). When there is no prior information on the medium, iterative inverse problems can be used (Cox et al. 2012, Hochuli et al. 2016) to recover both absorption $\mu_a(\mathbf{r})$ and scattering coefficients $\mu_s(\mathbf{r})$, offering fluence compensation. Generally, inverse problems are complex and computationally demanding and have requirements regarding the measurements and the model to converge to the right solution. Approaches attempting to reduce the dimensionality of the problem using learning ensembles look promising but might lack generality (Tzoumas et al. 2016). Alternatively, photoacoustic imaging has been coupled with other modalities such as diffuse optical tomography (Bauer et al. 2011) or acousto-optic imaging (Daoudi et al. 2012) to perform fluence compensation but these combinations are limited in resolution and require additional equipment.

There exists no direct imaging method capable of imaging fluence in optically heterogeneous environments using a single device and/or without the use of inverse models. We propose a new multi-modal approach to decouple fluence and optical absorption in the photoacoustic measurement.

Interestingly, ultrasound and photoacoustic imaging can be performed using the same equipment (Niederhauser et al. 2005, Kolkman et al. 2008, Garcia-Uribe et al. 2015, Kim et al. 2016, van den Berg et al. 2016, Fenster et al. 2001). Ultrasound B-mode images can provide complementary anatomical information to PA imaging which has been used to enhance quantitative PA reconstruction through regional segmentation furnishing priors (Yang et al. 2020).

Blood vessels, which are sensitive to both US and PA imaging, are ubiquitous in living tissues, from large vessels to capillary beds, filling all the organs. Beyond ultrasound B-mode images, Ultrasound Doppler techniques can image blood vessels specifically from the decorrelation induced by flow. Its combination with PA imaging uniquely provides optical and flow dynamics characterization of blood (Robin et al. 2021,

Godefroy et al. 2023). Nevertheless, there are no studies coupling the quantitative blood information provided by ultrasound Doppler imaging with PA imaging. In other words, we present a first demonstration of combining quantitative information from these two imaging modalities.

Among other Doppler techniques, Ultrasound Power Doppler (UPD) provides fractional blood presence in a pixel (Rubin et al. 1995), which, assuming a uniform hematocrit, is proportional to the blood volume or partial volume of vessels in the pixel (Macé et al. 2011), or equivalently, fractional vessel density.

Photoacoustic fluctuation imaging (PAFI) is analogous to Power Doppler for photoacoustic imaging and allows to solve the limited visibility issues (Vilov et al. 2020). The PAFI technique was recently extended to spectroscopy for SO_2-imaging, and combined to UPD (Godefroy et al. 2023). Like ideal conventional PA imaging, PAFI provides images proportional to the absorbed energy (product of local fluence and absorption coefficient). After discretizing the medium to a grid related to the imaging resolution, there exist situations where the imaged absorption is an effective absorption, spatially averaged at the resolution of the system. This happens when imaging objects smaller than the resolution such as small vessels or capillary networks. The effective absorption can be viewed as a decimation of a true high-resolution absorption and it directly depends on the local vessel density. In this case of unresolved vessels, PAFI can not decouple partial volume effects from fluence. We propose the combination of PAFI and UPD to decouple fluence and absorption within blood vessels.

After exposing some theory, we introduce a full-PSF filter and its formalism, enabling the coupling of UPD and PAFI for 3D fluence imaging. The technique is demonstrated in simulation and experimentally in a flow phantom. Given its shown accuracy, this technique could serve real-time applications or inverse problems in photoacoustic imaging in the future.

2. Theory and principles

2.1. Medium model

Photoacoustic fluctuation imaging (PAFI) solves the visibility artifacts and provides images related to the absorbed energy density (Vilov et al. 2020, Godefroy et al. 2023). The theoretical framework employed in PAFI is recalled here and is applied to US Power Doppler. We suppose a medium composed of blood vessels filled with flowing red blood cells (RBCs). The binary function $f(\mathbf{r})$ describes blood vessel presence. Inside blood vessels, a fluctuating function $g_k(\mathbf{r})$ describes the presence of RBCs. RBCs are the objects generating contrast for both ultrasound and photoacoustic imaging and the relevant physical properties of RBCs are respectively acoustic impedance variation ΔZ and optical absorption μ_{RBC}, which are considered uniform within each RBC but can vary over the imaged domain. Particularly, μ_{RBC} is generally modulated by local oxygenation. The system's point spread function (PSF) is here defined in the image

space. The PSF $h(\mathbf{r}', \mathbf{r})$ represents the image of the system obtained from a point diffuser for ultrasound imaging and from a point absorber for PA imaging. The shape and amplitude of the PSF depend on the imaging system itself (transducer, electronics), but also on the employed reconstruction algorithm. Here, we consider the case where the PSF varies within the imaged region. This non-stationary PSF is expressed with two spatial coordinates $\mathbf{r}'$ representing where the point sources are positioned and $\mathbf{r}$ representing the reconstructed image coordinates. These PSFs are complex since they are obtained from IQ-demodulated or Hilbert-transformed signals, enabling classical envelope detection (Berthon et al. 2018, Godefroy et al. 2023).

2.2. PAFI theory in turbid media and non-stationary PSFs

From this model and according to previously reported studies (Vilov et al. 2020, Godefroy et al. 2023), we can express the mean PA image with a generalization to non-stationary PSFs. The mean PA image is expressed as:

$$m_{\mathrm{PA}}(\lambda, \mathbf{r}) = \Gamma(\mathbf{r})\mu_{\mathrm{RBC}}(\lambda, \mathbf{r}) \quad \times\Phi(\lambda, \mathbf{r}) \quad \times\eta(\mathbf{r}) \quad \times \int h_{\mathrm{PA}}(\mathbf{r}, \mathbf{r}')f(\mathbf{r}')\mathrm{d}\mathbf{r}' \qquad (1)$$

where $\Gamma(\mathbf{r})$ is the Gruneisen parameter and $\mu_{\mathrm{RBC}}(\lambda, \mathbf{r})$ is the red blood cells absorption. These first terms are related to the medium ability to convert light into sound. $\Phi(\lambda, \mathbf{r})$, the light fluence, represents the excitation term. $\eta(\mathbf{r})$ denotes the volume fraction, which is related to the red blood cell statistics. Finally, we find the object-PSF integral term.

Demonstrations from (Vilov et al. 2020, Godefroy et al. 2023) can then be used to obtain the variance image (PAFI):

$$\sigma^2_{\mathrm{PA}}(\lambda, \mathbf{r}) = \Gamma^2(\mathbf{r})\mu^2_{\mathrm{RBC}}(\lambda, \mathbf{r})\times \Phi^2(\lambda, \mathbf{r})\times \eta(\mathbf{r})\, W[\eta(\mathbf{r})]V_{\mathrm{RBC}}(\mathbf{r})\times \int |h_{\mathrm{PA}}|^2(\mathbf{r}, \mathbf{r}')f(\mathbf{r}')\mathrm{d}\mathbf{r}' \qquad (2)$$

Compared to equation (1), new statistical terms appear: $V_{RBC}(\mathbf{r})$ is the red blood cell volume, W is the packing factor which depends on the volume fraction $\eta(\mathbf{r})$. In PAFI, besides the squared version of some parameters, we can notice that the equation holds the terms related to the same information as in the mean PA image.

2.3. Power Doppler theory

Ultrasound imaging of blood flow relies on its dynamics. While quantitative backscattering of red blood cells has been widely studied (Mo & Cobbold 1992, Cloutier & Qin 1997), no quantitative theory including the imaging part has been proposed. A quantitative theory is detailed in the supplementary materials. We first express the mean image of blood flow to compare with the mean PA image:

$$m_{\mathrm{US}}(\mathbf{r}) = \frac{\Delta Z(\mathbf{r})}{Z_0}\times \quad P_i(\mathbf{r})\times \quad \eta(\mathbf{r})\times \quad \int h_{\mathrm{US}}(\mathbf{r}, \mathbf{r}')f(\mathbf{r}')\mathrm{d}\mathbf{r}' \qquad (3)$$

where $\frac{\Delta Z(\mathbf{r})}{Z_0}$ is the relative mean impedance fluctuation induced by a single red blood cell, P_i is the incident acoustic pressure, η is the volume fraction, h_{US} is the US imaging PSF and $f(\mathbf{r})$ defines the blood vessels. Similarly to the PA version, we find in this equation the product between medium characteristics, excitation amplitude, statistics of red blood cells and object-PSF integral.

An Ultrasound power Doppler (UPD) image consists in integrating the fluctuations observed from the blood flow. The resulting UPD image expression is:

$$\sigma^2_{\mathrm{US}}(\mathbf{r}) = \left(\frac{\Delta Z(\mathbf{r})}{Z_0}\right)^2 \times \quad P_i^2(\mathbf{r}) \times \quad \eta(\mathbf{r}) W[\eta(\mathbf{r})] V_{\mathrm{RBC}}(\mathbf{r}) \times \quad \int |h_{\mathrm{US}}|^2(\mathbf{r}, \mathbf{r}') f(\mathbf{r}') \mathrm{d}\mathbf{r}' \quad (4)$$

where, as in equation (2), V_{RBC} is the red blood cell volume and $W(\eta)$ is the packing factor. Interestingly, formula (4) and (2) have the same structure which enables further development in this work.

2.4. Discretization of the model to a matrix formalism

A discretization of the imaged domain is both performed in the source coordinates $\mathbf{r}'$ and image coordinates $\mathbf{r}$ with the same spatial grid (Wang et al. 2010). The discretization should prevent the loss of information for the PSFs with sufficient spatial sampling. The spatial grid is formed with steps of $\lambda/2$ where λ is the central wavelength of the detector. The discretized object $F = f(\mathbf{r}'_j)$ can lose information when the continuous object contains spatial frequencies exceeding the spatial Fourier support of the PSFs. In this case, the object is unresolved but still contains quantitative information which we exploit in this study. Voxel values of F are no longer binary like $f(\mathbf{r}')$ but are equal to fractional vessel densities within each voxel. Defining the matrices $H_{PA} = \{h_{PA}(\mathbf{r}_i, \mathbf{r}'_j)\}$ and $H_{US} = \{h_{US}(\mathbf{r}_i, \mathbf{r}'_j)\}$, the matrix version of equations (1) and (3) are given by:

$$\begin{aligned} m_{\mathrm{PA}}(\lambda, \mathbf{r}_i) = \quad & \Gamma(\mathbf{r}) \mu_{\mathrm{RBC}}(\lambda, \mathbf{r}_i) \times \quad \Phi(\lambda, \mathbf{r}_i) \times \quad \eta(\mathbf{r}_i) \times \quad [H_{\mathrm{PA}} F](\mathbf{r}_i) \\ m_{\mathrm{US}}(\mathbf{r}_i) = \quad & \frac{\Delta Z(\mathbf{r}_i)}{Z_0} \times \quad P_i(\mathbf{r}_i) \times \quad \eta(\mathbf{r}_i) \times \quad [H_{\mathrm{US}} F](\mathbf{r}_i) \end{aligned}$$

Equivalently, by defining $Q_{PA} = \{|h_{PA}(\mathbf{r}_i, \mathbf{r}'_j)|^2\}$ and $Q_{US} = \{|h_{US}(\mathbf{r}_i, \mathbf{r}'_j)|^2\}$, equations (2) and (3) can be written:

$$\sigma^2_{\mathrm{PA}}(\lambda, \mathbf{r}_i) = \quad \Gamma^2(\mathbf{r}_i) \mu^2_{\mathrm{RBC}}(\lambda, \mathbf{r}_i) \times \quad \Phi^2(\lambda, \mathbf{r}_i) \times \quad \eta(\mathbf{r}_i)\, W[\eta(\mathbf{r}_i)] V_{\mathrm{RBC}}(\mathbf{r}_i) \times \quad [Q_{\mathrm{PA}} F](\mathbf{r}_i) \quad (5)$$

$$\sigma^2_{\mathrm{US}}(\mathbf{r}_i) = \quad \left(\frac{\Delta Z(\mathbf{r}_i)}{Z_0}\right)^2 \times \quad P_i^2(\mathbf{r}_i) \times \quad \eta(\mathbf{r}_i) W[\eta(\mathbf{r}_i)] V_{\mathrm{RBC}}(\mathbf{r}_i) \times \quad [Q_{\mathrm{US}} F](\mathbf{r}_i) \quad (6)$$

where the ^{2} sign defines element-wise square exponent. Q_{US} and Q_{PA} contain all the reconstructed PSFs of UPD and PAFI. This formalism allows to introduce the combination of the two modalities.

2.5. Combination of Power Doppler and PAFI

The power Doppler formula (6) is very similar to the PAFI formula (5). An important difference is in the convolution term: although the imaged object is the same, it is imaged with a different PSF, resulting in different axial and lateral resolutions. Note that the PSFs are by definition positive and real and that the phase information of the acoustic signals is no longer present. We propose equalizing the resolutions of the two techniques. This equalization is more stable if the resolution of the higher resolution modality is degraded to the one of the lower. UPD benefits from both focus in emission and reception whereas PAFI is only obtained after focus in emission. Hence, UPD resolution is higher than PAFI. Thus, we choose to degrade the resolution of UPD to the one of PAFI. We define the PSF filter G enabling this operation:

$$G = \underset{\tilde{G}}{\operatorname{argmin}} \|\tilde{G}.Q_{US} - Q_{PA}\|^2 \tag{7}$$

Obtaining G requires solving N_p^2 linear coupled equations where N_p is the number of reconstructed points in the image. Once G is computed, it can be applied to the UPD image to obtain the PSF-filtered UPD image:

$$\tilde{\sigma}^2_{US} = G.\sigma^2_{US} \tag{8}$$

$\tilde{\sigma}^2_{US}$ and σ^2_{PA} end up having the same PSF-object integral allowing the introduction of the fluence imaging method.

2.6. Principle of fluence imaging

Blood vessels regions are defined at the UPD resolution, as a domain M_{BV} satisfying $\mathbf{r} \in M_{BV}$ if $\tilde{\sigma}^2_{US}(\mathbf{r}) > \epsilon$, where ϵ is a threshold set on the UPD image amplitude. We define the fluence in blood vessels $\Phi_{BV}(\mathbf{r})$ as:

$$\Phi_{BV}(\mathbf{r}) = \begin{cases} \Phi(\mathbf{r}) & \text{if } \mathbf{r} \in M_{BV} \\ 0 & \text{otherwise} \end{cases} \tag{9}$$

The ratio of a PAFI image and a filtered UPD image within blood vessels ($\forall \mathbf{r} \in M_{BV}$) becomes:

$$\frac{\sigma^2_{PA}(\lambda, \mathbf{r})}{\tilde{\sigma}^2_{US}(\mathbf{r})} = \frac{\Gamma(\mathbf{r})^2 \mu_{RBC}(\lambda, \mathbf{r})^2}{P_i(\mathbf{r})^2 (\Delta Z(\mathbf{r})/Z_0)^2}.\Phi_{BV}(\lambda, \mathbf{r})^2 \tag{10}$$

The fluence in blood vessels ($\forall \mathbf{r} \in M_{BV}$) can be expressed:

$$\Phi_{BV}(\lambda, \mathbf{r}) = \frac{P_i(\mathbf{r}) \Delta Z(\mathbf{r})/Z_0}{\Gamma(\mathbf{r}) \mu_{RBC}(\lambda, \mathbf{r})}.\frac{\sigma_{PA}(\lambda, \mathbf{r})}{\tilde{\sigma}_{US}(\mathbf{r})} \tag{11}$$

One main feature given by this approach is that the fluence formula is independent of the statistical properties of red blood cells, $\eta(\mathbf{r})$, $W(\eta(\mathbf{r}))$ and $V_{RBC}(\mathbf{r})$. As $\eta(\mathbf{r})$ can vary with the vessel size (Pries et al. 1986), the independence to the quantity $\eta(\mathbf{r})W(\eta(\mathbf{r}))$ is highly valuable.

To obtain a fluence image, the pre-factor $\frac{P_i(\mathbf{r})\Delta Z(\mathbf{r})/Z_0}{\Gamma(\mathbf{r})\mu_{RBC}(\lambda,\mathbf{r})}$ has to be known at each position. Incident pressure $P_i(\mathbf{r})$ is the result of the excitation of the transducer that can be calibrated and the acoustic attenuation of the medium. We consider that this quantity can be determined and P_i as uniform in our case. $\Delta Z(\mathbf{r})/Z_0$ corresponds to the mean RBC acoustic properties which can be considered uniform as well as the Gruneisen coefficient. Finally, $\mu_{RBC}(\lambda,\mathbf{r})$ can depend on blood oxygenation and thus on the position, with the exception of the isosbestic wavelength of $\lambda_0 = 800nm$. Under these conditions, one obtains the fluence imaging expression:

$$\Phi_{BV}(\lambda_0,\mathbf{r}) = \frac{P_i\Delta Z/Z_0}{\Gamma\mu_{RBC}(\lambda_0)}.\frac{\sigma_{PA}(\lambda_0,\mathbf{r})}{\tilde{\sigma}_{US}(\mathbf{r})} \tag{12}$$

This expression is the main theoretical result of this work. We further describe how we apply this framework to simulated and experimental images.

3. Methods

3.1. Model-based matrix approach

Q matrices are computed from forward matrices K obtained from simulations that gather all the time responses of the individual grid point. For reconstruction, we use the matrix backprojection algorithm corresponding to matrix products $K^\dagger K$. All the details for the computation of Q matrices and G filter are given in the Supplementaries.

3.2. Phantoms for numerical validation

To validate our theory with simulations, we use an object F containing a set of cylinders mimicking blood vessels with varying diameters. Notably, the smallest diameter is intentionally chosen to be smaller than the PSF. These cylinders are oriented along the axes of either the XY or YZ planes. Assuming background medium and blood properties ($\mu_a = 0.25$ cm^{-1}, $\mu_s' = 1.2$ cm^{-1} and $\mu_{a,\text{blood}} = 4.3$ cm^{-1}), a Monte Carlo simulation (described in 3.4) is executed to generate the fluence map, which is subsequently masked by the object to isolate the fluence within the vessels.
Our aim is to account not only for isolated vessels but also for the anatomical presence of multiple vessels within the same pixel, reflecting the partial volume effects. Hence, for a second simulation, we selected a 3D *in vivo* image of a mouse brain acquired using ultrasound-localization microscopy (Demeulenaere et al. 2022). Firstly, the image is binarized to obtain a high-resolution segmented vessel network $f(\mathbf{r})$. The image is decimated from a 20 μm grid step to our imaging grid step of 90 μm. The decimation

implies an anti-alias low pass filter followed by undersampling. Fluence is simulated according to section 3.4 assuming uniform scattering (μ_s) without absorption.

3.3. Phantoms for experimental validation: flow phantoms in light scattering medium

For a first experimental demonstration of the proposed approach, we fabricated two phantoms composed of three glass capillaries each (Capillary Tube Supplies Ltd, UK), distributed at different heights and positions in a 3D-printed frame. While the same capillary size is chosen for the first phantom (inner diameter $D = 0.6$ mm), capillaries of inner diameters $D_1 = 0.15$ mm (smaller than PSF size), $D_2 = 0.20$ mm (comparable to PSF size) and $D_3 = 0.6$ mm compose the second one. The wall thickness is 10 μm, regardless of their size which implies constant acoustic/optical loss for all capillary sizes. The three capillaries were connected in series with PTFE tubing and perfused with a 1%-BSA solution of PBS for surface preparation. For each experiment, we used blood provided by the French Blood Bank (Etablissement Français du Sang, EFS). Prior to experiments, blood is re-oxygenated for 1h using an oxygen balloon. A peristaltic pump assured a continuous flow in the first phantom. In the second phantom, blood flow was induced via two syringe pumps with an adapted flow rate for capillaries of different sizes. The phantom was held in a tank containing a tissue-mimicking light-scattering medium. A basic sketch of the phantom is depicted in Fig.1B. This medium consisted of diluted milk and China ink, calibrated to replicate a μ_a of 0.25 cm^{-1} and a μ_s' within a range of 1.1 to 2 cm^{-1}. Before dilution, the ink was sonicated and syringe-filtered with a 40 μm pore size to avoid floating ink aggregates compromising image visualization. Given that the capillaries in the phantoms were confined to a specific region within the imaged volume, the G filter was computed on a sub-volume of $[14\times70\times89]$ voxels, corresponding to $1.3 \times 6.3 \times 8$ mm^3.

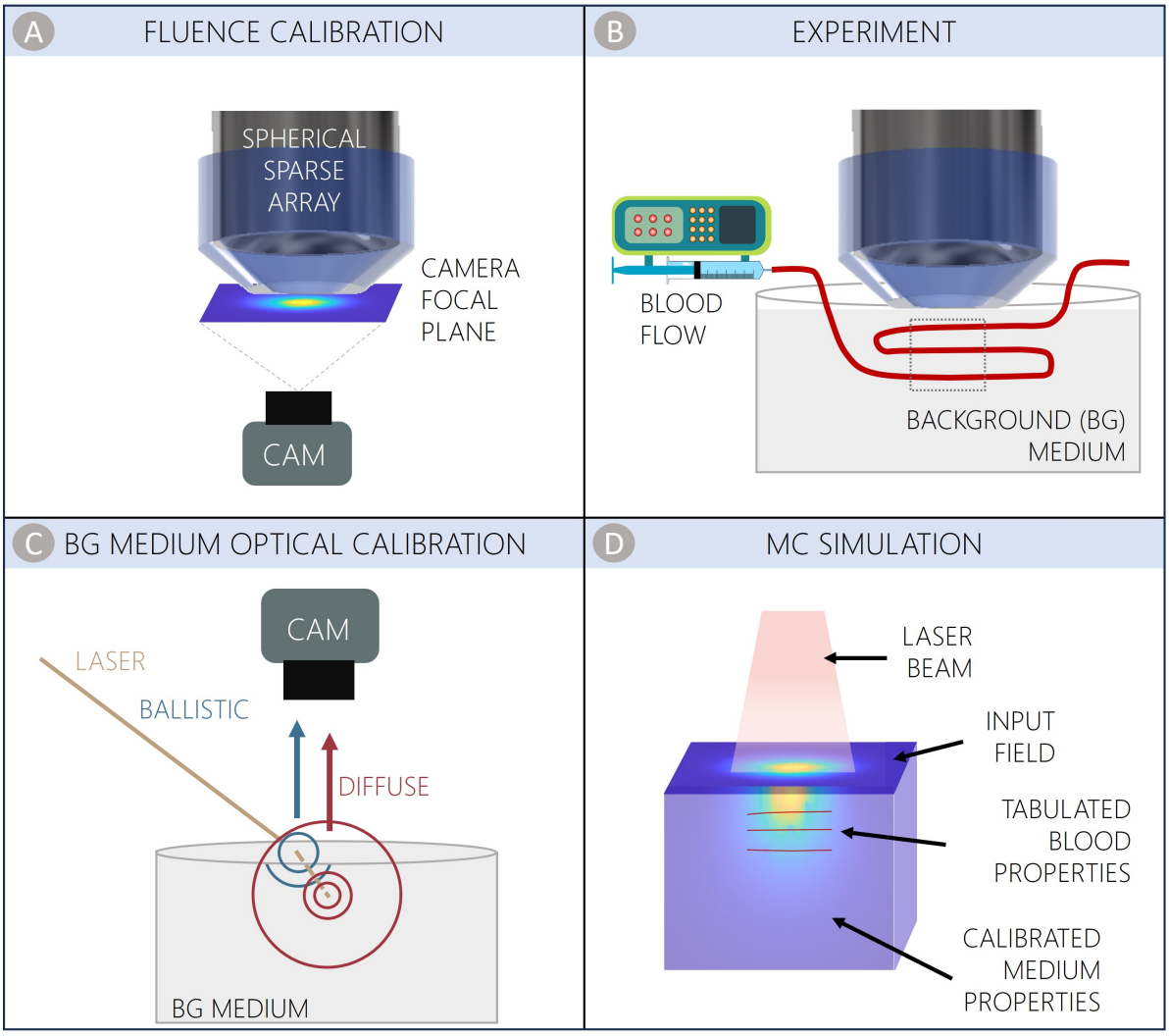

Figure 1: Illustration of all the methods used. A) Fluence calibration: fluence imaging at the surface of the contact cone, experimentally measured with a camera. B) Experimental setup: imaging of a flow phantom positioned in a light-scattering medium. C) Background medium optical calibration: diffuse reflectance technique with an oblique angle employed after each experiment to determine the reduced scattering coefficient of the background medium. D) Monte Carlo simulation of the ground truth fluence using the input field given by the step A, tabulated blood properties for the capillaries at the experimental positions and the calibrated medium properties given by step C.

3.4. Simulation of photon transport as ground truth fluence

A fluence calibration was performed by experimentally measuring the fluence at the surface of the contact cone using a CMOS camera (Basler ACA1300200um) coupled with a camera objective, as shown in Fig.1A. While this calibration needs to be performed only once, the calibration of the optical properties of the background medium was conducted after each experiment. To this purpose, we employed a diffuse reflectance

technique with an oblique angle to determine the reduced scattering coefficient of the imaged light-scattering medium (Wang & Jacques 1995). The corresponding setup is summarized in Fig.1C.

Knowing the incident fluence pattern and the optical properties of our phantom enabled the simulation of ground truth fluence as shown in Fig. 1D. The light transport simulation is done using MCXlab (Fang & Boas 2009), with a MATLAB interface. MCXLAB is a well-established Monte Carlo optical transport modeling tool that approximates efficiently the radiative transport equation with a GPU implementation. The previously mentioned characterizations supply essential input parameters for each ground truth simulation. To complete the characterization of the medium, the capillary positions were derived from the experimental images, and standard tabulated blood optical properties applied to them.

During experimental acquisitions, a calibrated photodiode records laser pulse energy, as described in an earlier contribution (Godefroy et al. 2023). This eventually allows normalizing simulated fluences to $\mathrm{mJ/cm^2}$.

3.5. Experimental setup, data acquisition and image reconstruction

Samples were illuminated from the top (see Fig.1B), with a pulsed laser (Spitlight DPSS 250, Innolas) at $\lambda = 800$ nm, with a repetition rate of 100 Hz and a laser pulse duration of 5 ns. The light was delivered via a fiber bundle passing through the center of a custom 256-channel matrix array (Imasonic, France, Voray-sur-l'ognon). It features a center frequency of 8 MHz, a focal distance of 35 mm and a field of view of approximately $8 \times 8 \times 8$ $\mathrm{mm^3}$. The transducer was coupled with a cone and connected to a 256-channel acquisition electronics (High Frequency Vantage 256, Verasonics, USA). Our research group has previously provided a detailed description of these setup and instrumentation (Godefroy et al. 2023).

The collected radio-frequency (RF) data comprised N = 2700 repeated PA acquisitions at a frequency of 100 Hz, interleaved with multiple US acquisitions at a repetition rate of 200 Hz. To reconstruct 3D images from RF signals, we employed model-based matrix backprojection for both PA and US images. US images were generated by compounding the backprojected images from n_{Tx} successive acquisitions, each corresponding to the ultrasound emission by one of the $n_{Tx} = 10$ selected transducer elements (Montaldo et al. 2009). On the other hand, a single photoacoustic image was derived from each laser shot. Subsequently, a singular-value-decomposition (SVD) filter was applied to the stack of 2700 3D images, following a previously reported methodology (Vilov et al. 2020, Godefroy et al. 2023). PAFI and UPD images were computed via the standard deviation of the stack of images along the temporal dimension. Before applying the PSF corrections and calculating the ratio of the two images, the electronic noise was subtracted from each variance image. Unlike the previously employed delay-and-sum reconstruction (Godefroy et al. 2023), the variance of backprojected noise is non-uniform and we describe the employed method to estimate the noise pattern in the

supplementary.

3.6. Alternative approach and PSF partial corrections

A simpler approach, relying on the information given from PAFI only and neglecting any potential partial volume effect, was implemented. This naive resultant fluence, henceforth denoted as PAFI Φ_{BV}, basically supposes that the effective blood absorption is uniform and was computed as:

$$\Phi_{BV,PAFI} = \sigma_{PA} \oslash \left[\sum Q_{PA} \right]^{\circ \frac{1}{2}} \tag{13}$$

where $\oslash$ is the Hadamard division, $\sum Q_{PA}$ is a column-wise summation and $^{\circ \frac{1}{2}}$ refers to element-wise square root.

Along with the demonstration of the PAFI & UPD combination, we demonstrate the need for the PSF-filter in our multi-modal approach by comparing it with three computationally less demanding partial corrections, in addition to the case of no correction. Methods and results regarding these partial corrections are discussed in the supplementary section.

4. Results

4.1. Fluence imaging in simulated phantom including multi-scale isolated vessels

As an illustration, we consider a numerical simulation of a medium having given binary $F(\mathbf{r})$ map (Fig.2a) with uniform $\mu_a(\mathbf{r})$ and $\mu_s(\mathbf{r})$ in the background. The resulting fluence map is obtained through Monte-Carlo modeling (see section 3.4) and shown in Fig.2b).

PAFI and UPD images reveal some differences due to probe sensitivity, resolution, and fluence decay (2c-d). The PSF-filter G is employed to obtain the resolution-degraded $\tilde{\sigma}_{US}(\mathbf{r})$ (Fig.2e). A mask defined from $\tilde{\sigma}_{US}(\mathbf{r})$ is applied on the fluence maps, to obtain the true fluence in blood vessels (Φ_{BV}, Fig.2f).

The naive estimation of fluence, PAFI Φ_{BV}, is given in Fig.2g. The resulting fluence distribution in blood vessels is almost exact in vessels larger than the PSF, but some surprising discrepancies are also present. To quantify these discrepancies, we computed the root mean square error normalized by the true values (NRMSE), which was estimated to be 16% when considering the entire capillary network. Let us now focus only on vessels smaller than the PSF, such as the one circled in Fig.2 f, g, and h. The zoomed-in versions presented in the boxes (Fig.2 f', g', and h') clearly show that PAFI alone fails to decouple fluence from partial volume effects, leading to inaccurate values (NRMSE=55.3 %± 5.5% when considering all the unresolved capillaries).

Using the two modalities, PAFI&UPD Φ_{BV} matches the True Φ_{BV}, (global NRMSE=1.85%), including in unresolved vessels (NRMSE= 0.4%±0.1%). Using this

numerical case, we show the effects of vessel size and fluence are effectively decoupled using the described method.

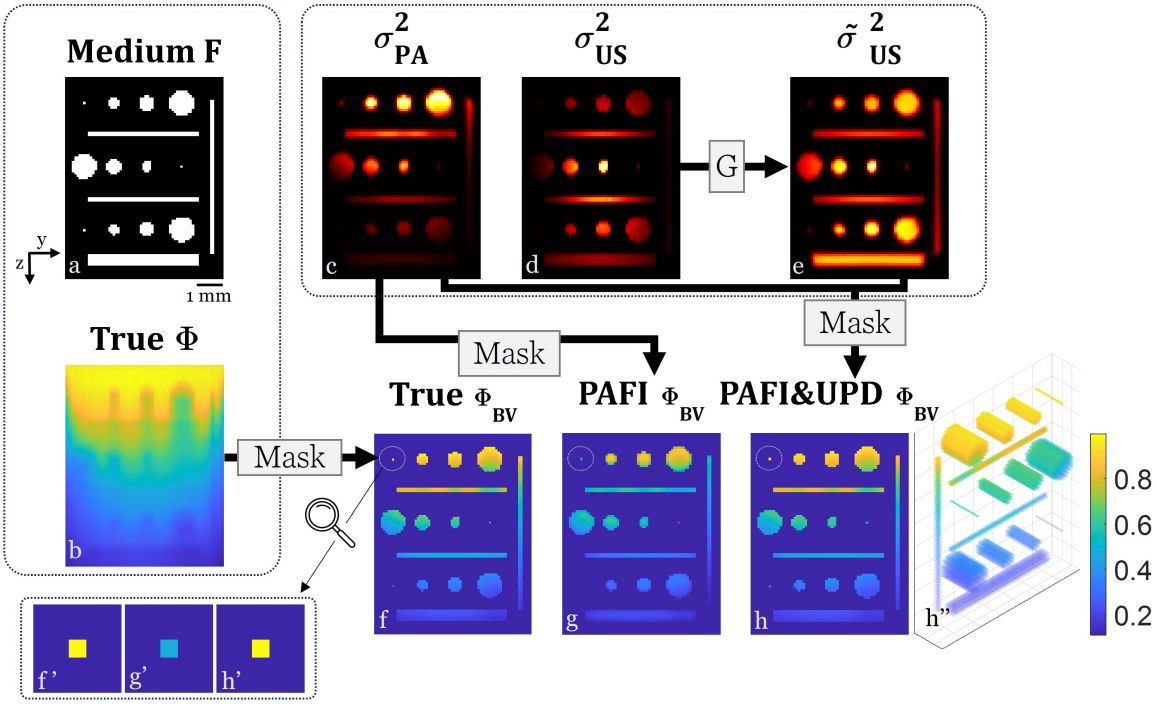

Figure 2: Fluence Imaging Validation in Simulated Phantom. a) Binary medium; b) Monte Carlo simulated fluence image; c-e) c) PAFI image; d) UPD image; e) PSF-filtered UPD image; f) Masked Monte Carlo simulated fluence: fluence in blood vessels; g) PAFI fluence in blood vessels, derived from the information in PAFI image only; h) PAFI & UPD fluence in blood vessels, computed through the proposed fluence imaging approach. f'-h') Focus on one of the unresolved vessels. Slices of the 3D images along the X-direction are represented in a-h', whereas h" provides a 3D comprehensive view of the fluence distribution within the numerical phantom.

4.2. Fluence imaging in simulated brain including multiscale vessels network

The top row of Fig. 3 illustrates PAFI, UPD, and its filtered version images (c-e), originating from the decimated ULM mouse brain image (b), obtained from (a), as described in 3.2. Once again, the results in the bottom row highlight the accuracy of PAFI&UPD Φ_{BV} in both big vessels and unresolved capillary bed. The observed error is 1.86%, which is 18 times smaller than the error incurred with the naive use of PAFI, where a lower fluence estimation in the unresolved objects and some discrepancies in the larger ones are displayed. Using this numerical case, we generalize the previous result on unresolved capillary beds.

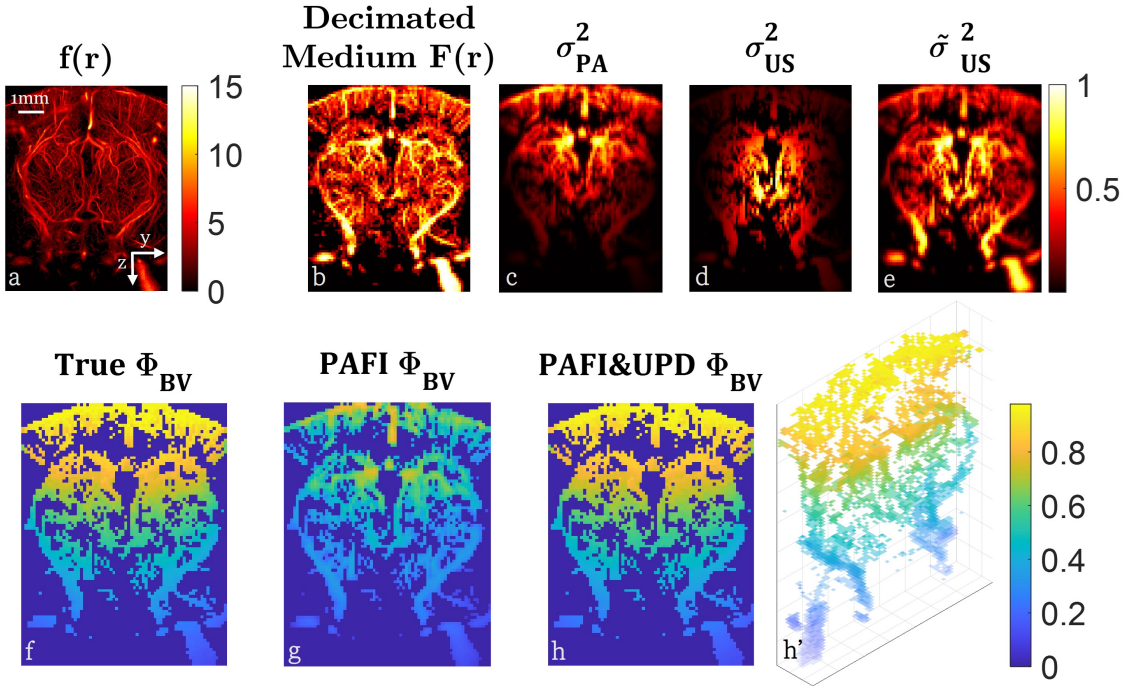

Figure 3: Fluence Imaging Validation in Simulated Brain. a) Image of a mouse brain acquired through ultrasound-localization microscopy (ULM); b) Decimated ULM image, aligned with our imaging spatial grid; c) PAFI image; d) UPD image; e) PSF-filtered UPD image; f) Monte Carlo simulated fluence, used as ground truth; g) PAFI fluence in blood vessels; h) PAFI & UPD fluence in blood vessels. All the 3-D images are presented as maximum intensity projections (MIP) along the x-direction, except for h', which provides a 3D view of the fluence distribution within the brain.

4.3. PSF-Filter validation in experimental results

For two experiments with the two different phantoms described earlier (see Section 3.3), maximum intensity projections of σ^2_{US} (Fig.4a) and σ^2_{PA} (Fig.4c) after noise subtraction are presented. Fig.4b illustrates the PSF filtered $\tilde{\sigma}^2_{US}$. It has been previously established that PAFI and UPD have different lateral and axial resolutions (Godefroy et al. 2023). We experimentally illustrate these differences by plotting the lateral and axial profiles (along the green dashed axes) of two capillaries with inner diameters of 0.6 mm and 0.2 mm (Fig.4d-e'). As expected, the resolutions corresponding to σ^2_{US} are higher than those of σ^2_{PA}. As extensively discussed in this paper, the goal of our PSF filter is to accommodate the resolution differences between PAFI and UPD. Therefore, the primary goal of the experimental proof-of-concept was to validate the accuracy of the simulation-derived PSF filter when applied to experimental data. Besides visually confirming that the $\tilde{\sigma}^2_{US}$ and σ^2_{PA} profiles are closely overlapped, we computed their FWHM (Full Width at Half Maximum). This quantification is provided in Table 1. The overlapping is reflected in the smaller difference between the $\tilde{\sigma}^2_{US}$ and σ^2_{PA}, both for

lateral and axial values, compared to σ^2_{US} and σ^2_{PA}.

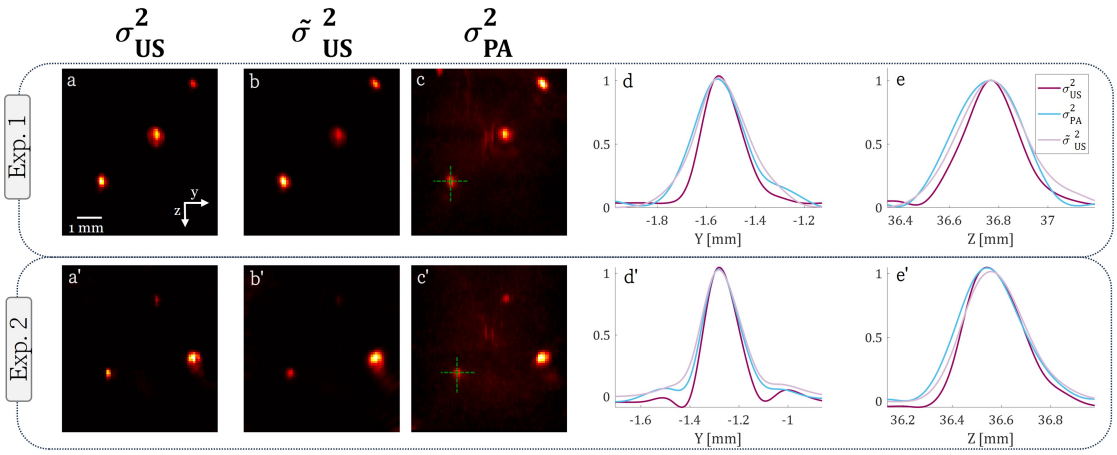

Figure 4: Validation of the PSF filter in Exp.1 and 2, using the first and second phantoms described in section 3.3. a-a': σ^2_{US}, b-b': PSF-filtered $\tilde{\sigma}^2_{US}$, c-c': σ^2_{PA}, d-d': lateral resolutions (along the green dashed horizontal axes), e-e': axial resolutions (along the green dashed vertical axes).

	FWHM [mm]	σ^2_{US}	$\tilde{\sigma}^2_{\text{US}}$	σ^2_{PA}
Exp.1	Lateral	0.19	0.24	0.24
	Axial	0.25	0.32	0.34
Exp.2	Lateral	0.15	0.18	0.17
	Axial	0.26	0.29	0.30

Table 1: Quantitative resolution analysis. Comparison of FWHM measurements pre and post-full PSF-filter for axial and lateral resolutions of each experiment (plots d,e,d',e' in Fig.4).

4.4. Fluence imaging in experimental results: relative qualitative and quantitative analysis

Fig.5 shows the experimental relative fluence within blood vessels. In this context, "relative" signifies that the experimental data, expressed in arbitrary units, were scaled by a specific factor denoted as $C_{opt,i}$, corresponding to the i^{th} experiment. This gain factor was obtained by fitting experimental values with ground truth values. $C_{opt,i}$ accounts for all the pre-factors in the PAFI-to-UPD ratio. In line with the simulated results section, we present in the first column, as a demonstration, the fluence images derived exclusively from PAFI and the naive assumption of constant blood density. The second column contains the results from the combination of PAFI & UPD. Images are represented as 2-D YZ slices obtained after averaging along the X-axis. A qualitative

comparison indicates that the fluence values in Fig.5-b.1 match with the values of the Monte Carlo simulated fluence map at the same positions, marked by the crosses (Fig.5-b.1). In this first experiment, where all capillaries exceed the PSF size, even the PAFI fluence (Fig.5-a.1), after colorbar normalization, produces comparable estimations.
The interest of our fluence imaging method becomes evident in the second experiment (Fig.5a-c.2). In this scenario, where the capillary within ROI#1 remains unresolved, only our PAFI & UPD technique offers a precise fluence estimation. In contrast, the naive PAFI fluence, as observed in simulations, significantly underestimates its value.
Results from six implemented experiments are summarized and quantitatively compared in Fig.6. In the correlation plot between the Monte Carlo simulated and the experimental Φ_{BV}, each data point denotes the mean value within the region of interest (ROI) around each capillary, considering only non-zero values. On one hand, the limitation of the naive PAFI Φ_{BV} is evident, with a large dispersion of the values, a Pearson coefficient r of 0.29 (Fig.6a) and a p-value equal to 0.23 ($\gg 0.05$). Indeed, in the best case across all experiments, the error is 14%. On the other hand, the PAFI & UPD approach provides fluence results that deviate from the simulated ones by a maximum of 6%. In this latter case, a strong correlation is observed, resulting in a r of 0.99 and a p-value of $1.5{\cdot}10^{-17}$ ($\ll 0.05$) (Fig.6b).

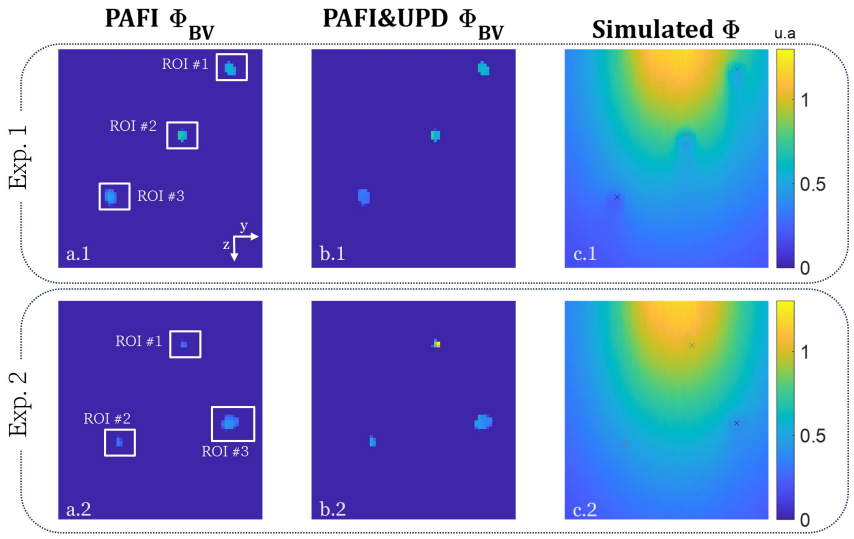

Figure 5: Experimental fluence images in blood vessels compared to simulated Monte Carlo fluence map (c.1-2). The three markers define the central position of each capillary, facilitating a visual comparison with the values of PAFI Φ_{BV} (a.1-2) and PAFI&UPD Φ_{BV} (b.1-2). The images are 2-D slices after averaging along the x-axis. For each capillary, a mean value within each ROI is then calculated, enabling quantitative analysis (see Fig 6).

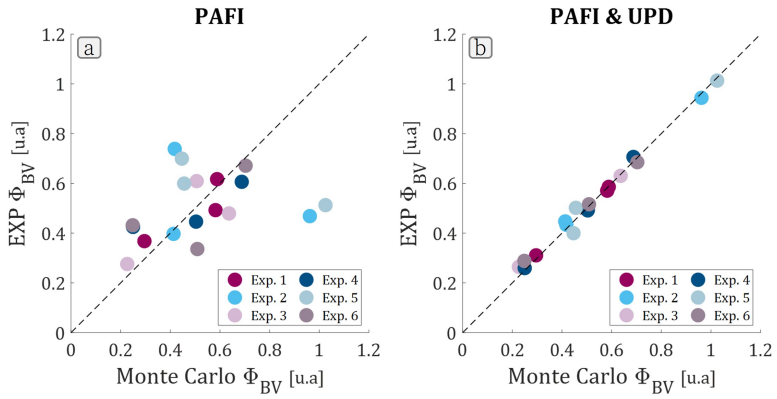

Figure 6: Correlation plot illustrating the relationship between simulated fluence (x-axis) and experimental fluence (y-axis) for estimations resulting from a) PAFI only and b) PAFI&UPD approach.

5. Discussion

Photoacoustic imaging measures the absorbed energy density, containing coupled local fluence and absorption. In vessels larger than the system resolution, hemoglobin absorption can be eventually considered known, leading to a determination of the fluence. However, observing vessels or vascular networks that are unresolved results in effective absorption coefficients that are locally heterogeneous. This leads to a coupling between local fluence and absorption, making it impossible to directly correlate the measurement with the local fluence. The use of inverse problems employing optical diffuse modeling becomes imperative for the quantitative determination of fluence and effective absorption. These inverse problems are complex and computationally demanding.

Therefore, in this article, we propose a direct imaging approach via the combination of photoacoustic fluctuation imaging (PAFI) and Ultrasound Power Doppler (UPD) to obtain quantitative fluence mapping in blood vessels. The theoretical UPD expression shares common terms with that of PAFI. At the isosbestic wavelength, the fluence imaging expression involves the ratio between PAFI and the filtered UPD. Indeed, a PSF filter is essential to equalize the resolution of both techniques. In this work, the PSF filter is developed in the context of 3D imaging and non-stationary PSFs. This method demonstrates theoretical independence from hematocrit, packing factor, and features of the imaged object, including vessel sizes, orientations, and vessel density. Importantly, it universally provides quantitative fluence. This approach uniquely decouples the effective absorption coefficient and fluence in unresolved blood vessels without using inverse problems. This decoupling is not achievable based on photoacoustic measurements only, as shown by our results involving the naive PAFI Φ_{BV}.

We initially demonstrate the technique in simulations involving isolated vessels of various sizes, including unresolved ones. Then, we extend our investigation to a simulation of

brain vasculature, defined from an Ultrasound Localization Microscopy high-resolution image. Finally, we experimentally validate the effectiveness of the PSF filter on vessels and provide quantitative fluence imaging, denoted as PAFI&UPD Φ_{BV}.

The full PSF-filter computation remains highly demanding. Hence, we implement and test the effectiveness of three additional faster corrections. These involve compensating only the PSF volume and/or amplitude, or simply treating the PSFs as spatially invariant. Experimental results, consistent with simulations, reveal discrepancies and non-uniformities within vessels, resulting in less accurate estimation, outperformed by our full PSF filter.

The fluence values depicted in Fig.5 and 6 are shown normalized. It ~~it~~ is important to note that these values were individually normalized with coefficients that slightly vary among experiments. In other words, the fluence values cannot be universally converted to mJ/cm^2 using a single coefficient. This variability is probably due to the SVD filtering steps applied to both the numerator and denominator of the fluence imaging formula. Further refinement of the method could be helpful for absolute dosimetry and metrologic applications. Some workaround could consist in obtaining a fluence estimation in a target located at the top surface of the sample, allowing a correct normalization.

We may question the applicability of this technique to 2D imaging. Since ultrasound and photoacoustic imaging exhibit distinct resolutions in elevation, compensating for the PSF differences in this direction would be necessary, which appears challenging without measuring a 3D object. We believe this approach is only valid for 3D imaging in the general case of arbitrary vessel directions.

Furthermore, the method needs to be investigated *in vivo*. For this purpose, a study on the sensitivity of the PSF filter to the speed of sound is crucial, and physiological motions will have to be minimized and/or corrected. The technique could be particularly interesting for application in capillary beds, necessitating a highly sensitive setup.

Finally, the combination of UPD with conventional photoacoustic (PA) imaging is out of the scope of this manuscript. A framework needs to be developed, but some challenges have to be addressed, such as the dependence on the packing factor $W[\eta(\mathbf{r})]$, which is present in UPD but not in conventional PA. In PAFI, the native specificity to the blood is particularly suited for this method whereas conventional PA is sensitive to additional static chromophores that may impact the results, even with hemoglobin being the dominant absorber at $800nm$ in most tissues. For this task, unmixing algorithms would have to be used, implying additional complexity. Eventually, the presented fluence imaging technique can be applied at any wavelength other than $800nm$ with the strong hypothesis that blood oxygen saturation is considered uniform throughout the imaged region, a condition that could be satisfied in various applications.

6. Conclusion

This study shows how combining the information contained in the PAFI and UPD modalities leads to fluence imaging, by universally decoupling effective blood absorption

from fluence, without the use of inverse problems.
The direct measurement of the spatial distribution of light within biological tissues could be relevant in photomedicine, where light is used for various diagnostic and therapeutic purposes.
Further than direct fluence imaging, we demonstrate that Ultrasound Power Doppler provides valuable information that can be integrated into quantitative photoacoustic imaging inverse problems. This integration could improve convergence in ill-posed photoacoustic inverse problems, addressing issues related to the non-uniqueness of solutions. This will be the focus of future works.
Beyond specific applications, this work lays the foundation to any work involving the coupling of quantitative information in Power Doppler and Photoacoustic imaging.

7. Aknowledgments

This work was supported by the Agence National de la Recherche (ANR) under the FULBOX project (ANR-21-CE19-0003-01).

Arridge S R 1999 Inverse problems **15**(2), R41.
Bauer A Q, Nothdurft R E, Erpelding T N, Wang L V & Culver J P 2011 Journal of biomedical optics **16**(9), 096016–096016.
Beard P 2011 Interface focus **1**(4), 602–631.
Berthon B, Morichau-Beauchant P, Porée J, Garofalakis A, Tavitian B, Tanter M & Provost J 2018 Physics in Medicine & Biology **63**(3), 03NT03.
Bu S, Liu Z, Shiina T, Kondo K, Yamakawa M, Fukutani K, Someda Y & Asao Y 2012 IEEE transactions on biomedical engineering **59**(5), 1354–1363.
Cloutier G & Qin Z 1997 Biorheology **34**(6), 443–470.
Cox B, Laufer J & Beard P 2009 in 'Photons Plus Ultrasound: Imaging and Sensing 2009' Vol. 7177 SPIE pp. 294–302.
Cox B, Laufer J G, Arridge S R & Beard P C 2012 Journal of biomedical optics **17**(6), 061202–061202.
Daoudi K, Hussain A, Hondebrink E & Steenbergen W 2012 Optics express **20**(13), 14117–14129.
Demeulenaere O, Bertolo A, Pezet S, Ialy-Radio N, Osmanski B, Papadacci C, Tanter M, Deffieux T & Pernot M 2022 EBioMedicine **79**.
Fang Q & Boas D A 2009 Optics express **17**(22), 20178–20190.
Fenster A, Downey D B & Cardinal H N 2001 Physics in medicine & biology **46**(5), R67.
Garcia-Uribe A, Erpelding T N, Krumholz A, Ke H, Maslov K, Appleton C, Margenthaler J A & Wang L V 2015 Scientific reports **5**(1), 15748.
Godefroy G, Arnal B & Bossy E 2023 Scientific Reports **13**(1), 2961.
Hochuli R, Powell S, Arridge S & Cox B 2016 Journal of biomedical optics **21**(12), 126004–126004.
Holmer C, Lehmann K S, Risk J, Roggan A, Germer C T, Reissfelder C, Isbert C, Buhr H J & Ritz J P 2006 Lasers in Surgery and Medicine: The Official Journal of the American Society for Laser Medicine and Surgery **38**(4), 296–304.
Hoshi Y & Yamada Y 2016 Journal of biomedical optics **21**(9), 091312–091312.
Jeng G S, Li M L, Kim M, Yoon S J, Pitre Jr J J, Li D S, Pelivanov I & O'Donnell M 2021 Nature communications **12**(1), 716.
Kim J, Park S, Jung Y, Chang S, Park J, Zhang Y, Lovell J F & Kim C 2016 Scientific reports **6**(1), 35137.
Kim M M & Darafsheh A 2020 Photochemistry and Photobiology **96**(2), 280–294.
Kolkman R G, Brands P J, Steenbergen W & van Leeuwen T G 2008 Journal of biomedical optics **13**(5), 050510–050510.

Macé E, Montaldo G, Cohen I, Baulac M, Fink M & Tanter M 2011 Nature methods **8**(8), 662–664.

Mo L Y L & Cobbold R S 1992 IEEE transactions on biomedical engineering **39**(5), 450–461.

Montaldo G, Tanter M, Bercoff J, Benech N & Fink M 2009 IEEE transactions on ultrasonics, ferroelectrics, and frequency control **56**(3), 489–506.

Niederhauser J J, Jaeger M, Lemor R, Weber P & Frenz M 2005 IEEE transactions on medical imaging **24**(4), 436–440.

Park S, Oraevsky A A, Su R & Anastasio M A 2019 in 'Photons Plus Ultrasound: Imaging and Sensing 2019' Vol. 10878 SPIE pp. 388–395.

Pries A, Ley K & Gaehtgens P 1986 American Journal of Physiology-Heart and Circulatory Physiology **251**(6), H1324–H1332.

Robin J, Özbek A, Reiss M, Dean-Ben X L & Razansky D 2021 IEEE Transactions on Medical Imaging **41**(4), 846–856.

Rubin J M, Adler R S, Fowlkes J B, Spratt S, Pallister J E, Chen J F & Carson P L 1995 Radiology **197**(1), 183–190.

Tzoumas S, Nunes A, Olefir I, Stangl S, Symvoulidis P, Glasl S, Bayer C, Multhoff G & Ntziachristos V 2016 Nature communications **7**(1), 12121.

van den Berg P J, Bansal R, Daoudi K, Steenbergen W & Prakash J 2016 Biomedical optics express **7**(12), 5081–5091.

Vilov S, Godefroy G, Arnal B & Bossy E 2020 Optica **7**(11), 1495–1505.

Wang K, Ermilov S A, Su R, Brecht H P, Oraevsky A A & Anastasio M A 2010 IEEE transactions on medical imaging **30**(2), 203–214.

Wang L & Jacques S L 1995 Appl. Opt. **34**(13), 2362–2366. Publisher: Optica Publishing Group.

Yang H, Jüstel D, Prakash J, Karlas A, Helfen A, Masthoff M, Wildgruber M & Ntziachristos V 2020 Photoacoustics **19**, 100172.